Radiative cooling in New York/New Jersey metropolitan areas by wildfire particulate matter emitted from the Canadian wildfires of 2023

Kelesidis, Georgios A.; Moularas, Constantinos; Parhizkar, Hooman; Tsiodra, Irini; Mihalopoulos, Nikolaos; Kavouras, Ilias; Korras-Carraca, Marios Bruno; Hatzianastassiou, Nikolaos; Georgopoulos, Panos G.; More Authors

Citation (APA)

Important note
To cite this publication, please use the final published version (if applicable).
Please check the document version above.

Radiative cooling in New York/New Jersey metropolitan areas by wildfire particulate matter emitted from the Canadian wildfires of 2023

Check for updates

Georgios A. Kelesidis [1,2] ✉, Constantinos Moularas[1,2], Hooman Parhizkar[1], Leonardo Calderon[3], Irini Tsiodra [4], Nikolaos Mihalopoulos[4,5], Ilias Kavouras[6], Marios-Bruno Korras-Carraca[7], Nikolaos Hatzianastassiou[7], Panos G. Georgopoulos[1], José G. Cedeño Laurent[1] & Philip Demokritou[1] ✉

Wildfire particulate matter from Canadian forest fires significantly impacted the air quality in the northeastern United States during the summer of 2023. Here, we used real-time and time-integrated instrumentation to characterize the physicochemical properties and radiative effects of wildfire particulate matter reaching the metropolitan areas of New Jersey/ New York during this extreme incident. The radiative forcing of $-352.4 \, W/m^2$ derived here based on the measured optical properties of wildfire particulate matter explains, to some extent, the ground level temperature reduction of about 3 °C observed in New Jersey/ New York City during this incident. Such negative radiative forcing in densely populated megacities may limit natural ventilation, increase the residence time of wildfire particulate matter and background air pollutants, exacerbating public health risks. This study highlights the importance of radiative effects from wildfire particulate matter in densely populated areas and their potential implications for climate, air quality and public health.

Climate change has increased dramatically the frequency, duration and intensity of wildfires with over 28,000 km² of land burnt every year in the US alone[1]. During the summer of 2023, wildfires burnt more than 66,000 km² of land in Canada. The wildfire particulate matter (WFPM) emitted by such extreme incidents impacts the climate[2] and the health[3] of communities living nearby, but it can be also transported over long distances and reach metropolitan areas (e.g. in New York State[4]) affecting millions of people.

In atmospheric science, the carbonaceous aerosols of WFPM are distinguished between black and organic carbon (OC), while the light absorbing component of OC is called brown carbon[5]. Black carbon particles consist of non-volatile elemental carbon (EC) and coagulate to form fractal-like agglomerates[6]. In contrast, brown carbon particles are typically spherical and contain mostly volatile and semi-volatile organic carbon (OC), as well as small amounts of EC[7–9]. Polycyclic aromatic hydrocarbons (PAHs)

generated during the wildfire adsorb on the surface of black and brown carbon and, as shown in emerging toxicological studies, can contribute to their bioactivity[10–12]. In this regard, exposure to WFPM has been linked with respiratory[12], cardiovascular[13] and neurological[14] disorders, but further epidemiological and mechanistic toxicological studies are required to quantify accurately its public health impact.

While the link of WFPM to human health has been made, its impact on the atmospheric dynamics and especially on the microclimate of major metropolitan areas and megacities is not well documented and studied[15]. The climate effect of WFPM is quantified by its direct radiative forcing, *RF*, that depends on its light absorption and scattering[16]. Black carbon agglomerates absorb strongly light[17] and further lift the wildfire plume extending its lifetime in the stratosphere and contributing to its long-distance atmospheric transport[18]. In contrast, brown carbon mostly scatters

¹Environmental and Occupational Health Sciences Institute, School of Public Health, Rutgers University, Piscataway, NJ, 08854, USA. ²Faculty of Aerospace Engineering, Delft University of Technology, Delft, 2629 HS, The Netherlands. ³Department of Environmental Sciences, School of Environmental and Biological Sciences, Rutgers University, New Brunswick, NJ, 08901, USA. ⁴Institute for Environmental Research and Sustainable Development, National Observatory of Athens, Lofos Koufou, Palea Penteli, Athens, 15236, Greece. ⁵Environmental Chemical Processes Laboratory, Department of Chemistry, University of Crete, Heraklion, 71003, Greece. ⁶Department of Environmental, Occupational and Geospatial Health Sciences, School of Public Health, City University of New York, New York, NY, 10018, USA. ⁷Laboratory of Meteorology and Climatology, Department of Physics, University of Ioannina, Ioannina, 45110, Greece. ✉e-mail: g.kelesidis@tudelft.nl; philip.demokritou@rutgers.edu

light due to its large OC content[8]. Freshly-emitted brown carbon particles may also absorb light depending on their chromophore and EC content[19], as well as on the volatility of their OC[20]. It is also well known that during atmospheric transport and aging under sunlight, brown carbon particles undergo photo-oxidation reactions with O_3 and OH[21]. This so-called photobleaching process can eliminate fairly rapidly the light absorption of brown carbon within 24 h of exposure to sunlight[21,22].

The direct *RF* induced by WFPM has been obtained only for a few wildfires by interfacing satellite observations with global climate models[23,24]. In these studies, it was shown that the direct *RF* of WFPM from wildfires in Russia was negative, indicating that wildfire emissions cool the atmosphere[23,24]. In addition, aircraft measurements were coupled with columnar models to estimate the *RF* induced by WFPM in Central US at various altitudes[25]. It is worth noting that the brown carbon particles identified at high altitudes (>5 km) absorbed strongly light and contributed to radiative warming whereas the majority of brown carbon particles were found at lower heights above the ground (<5 km) and resulted in strong radiative cooling[25]. However, there are no studies reporting the *RF* in major metropolitan areas and megacity environments during extreme wildfire events that generate large concentrations of WFPM.

In June 2023, WFPM from Quebec, Canada was transported to the Northeast US reaching New Jersey, New York City and other highly populated metropolitan areas. On June 7, the worst air quality level was recorded by the Environmental Protection Agency (EPA) in New York City with a 24-hour average $PM_{2.5}$ level of about 100 $\mu g/m^3$, while the $PM_{2.5}$ mass concentration measured in other major cities of Northeast US (e.g. Newark, NJ) also exceeded for three days the US 24-hour National Ambient Air Quality Standard (NAAQS; 35 $\mu g/m^3$) and the guidelines of the World Health Organization (WHO; 15 $\mu g/m^3$) by up to about 10 times. The impact of this WFPM incident on the public health in the New York area was documented in three recently published epidemiological studies[26–28]. In these studies, WFPM was linked to an increase of the asthma-related emergency department visits by about 44% in New York City[27] and 81.9% statewide[28] during the peak of this wildfire incident.

During the 2023 Canadian wildfire incident, WFPM was sampled and physicochemically characterized by the authors at the Rutgers University Piscataway Campus (about 70 km southwest of New York City) using real time and time-integrated instrumentation and analytical methods. The detailed physicochemical characterization of the WFPM using state-of-the-art equipment (see schematic in Supplementary Information: Fig. S1) enabled the accurate estimation of its direct *RF*. Most importantly, the radiative effects of wildfire smoke in such densely populated major metropolitan area were determined. In addition, the approach applied here can be used as an example for future studies since the intensity and frequency of wildfires and peri-urban forest fires are expected to increase in the coming years.

Results and discussion
WFPM transport and physicochemical characterization
The physicochemical properties of WFPM were monitored during the peak of the Canadian wildfire incident in New Jersey/New York City area on June 7, 2023 between 15:30 and 17:00 (EST) (peak event). Modeling of the air transport and dispersion reveals that WFPM measured on that day arrived within 24 h from the Canadian wildfire area that was about 800 km away from the sampling site (Fig. 1a: red squares). The fast transport of WFPM from Canada to Northeast US resulted in a large $PM_{2.5}$ mass concentration of 314.9 ± 27.9 $\mu g/m^3$ (Fig. 1b: red filled bar). This concentration is about an order of magnitude higher than the US 24-hour National Ambient Air Quality Standard (NAAQS) for $PM_{2.5}$ (35 $\mu g/m^3$). The mobility size distribution of WFPM measured on June 7 (Fig. 1c: solid line) reveals high concentrations of particles with mobility diameter, d_m, ranging from 100 to 300 nm. This is consistent with size distributions measured from fresh and denuded brown carbon particles[7–9].

The presence of brown carbon is further corroborated by the measured polyaromatic hydrocarbons (PAHs) adsorbed on the WFPM surface

(Fig. 1d). Retene, a standard molecular marker of wood combustion[29], is by far the main PAH identified here, consistent with previous retene measurements in wildfire smoke[10,11] and in line with the conifer nature of forests in this particular area of Canada. The large concentration of retene measured on June 7 may impact significantly public health, as retene promotes oxidative stress, mutagenic effects and cell necrosis[30].

In addition to retene, 8 out of the 16 EPA-prioritized PAHs were identified as part of the WFPM sampled here and include high molecular weight PAHs. These toxic PAHs exhibit high carcinogenic potency[31], raising concerns about potential health effects. It is worth noting that the 8 PAHs measured in this study have been also identified on the surface of brown carbon particles produced from wood combustion[31], while some of the 8 EPA-prioritized PAHs measured here have been measured in background aerosols from traffic pollution in Northeast US[32]. Our PAH findings are also in line with phenanthrene, benzo(e)pyrene and fluoranthene concentrations measured in WFPM from forest fires in Portugal[10], Canada[11] and western US[12]. It is also worth noting that the EC mass fraction of about 4 wt% (based on the total carbon mass) measured on June 7 (Fig. S2) is similar to that obtained from other prescribed and wildfire WFPM[33–36]. In this regard, the EC content[19], as well as some of the PAHs (e.g. pyrene and phenanthrene) and their photo-oxidation products[37] can contribute to the WFPM light absorption discussed in the next section.

The physicochemical properties of the sampled aerosols were also obtained the day after the peak of the incident on June 8, as well as on June 12, i.e. on a wildfire smoke-free day as the sampled air was transported mostly from the ocean (Fig. 1a: blue triangles). On June 8, WFPM arrived after 36 h from the Canadian wildfire spots (Fig. 1a: green circles). During this long transport time, WFPM is diluted and aged photochemically (as further confirmed in the next section). This reduced the $PM_{2.5}$ mass concentration at our sampling site to 44.6 ± 0.4 $\mu g/m^3$, as well as the number concentration of nanoparticles with $d_m = 100$–300 nm. Still, the mass and number concentrations measured on June 8 were substantially higher than those obtained on June 12 in the absence of wildfire smoke in the atmosphere (background condition).

Optical properties of WFPM
The light absorption and scattering of WFPM quantified by the absorption, b_{abs}, and scattering, b_{sca}, coefficients were monitored in real time using a photoacoustic extinctionmeter (PAX; Fig. 2). As mentioned above, WFPM contains mostly OC that scatters light and only a small fraction of EC (~4 wt%; Fig. S2) that predominantly absorbs and weakly scatters light. So, b_{sca} is one to two orders of magnitude larger than b_{abs} on all three sampling campaigns. This is further confirmed by the measured single scattering albedo, *SSA*, that is well above 0.9 on all three days of the sampling campaign. In particular, the *SSA* measured for WFPM on June 7 is consistent with those measured commonly for WFPM with similar EC and OC content[38–40]. Both b_{abs} and b_{sca} decrease significantly from June 7 to 8 and become similar to those measured for background aerosols on a smoke-free day (June 12, background).

The large reductions of b_{abs} and b_{sca} can be attributed to the large decrease of the $PM_{2.5}$ mass concentration, as well as on the variation of intrinsic particle properties, such as their EC[19] and OC[41] content, morphology[17] and degree of graphitization[42]. The latter can be quantified via the mass absorption cross-section, *MAC*, derived here by interfacing the measured b_{abs} and M[43]. That way, a WFPM *MAC* of 0.63 ± 0.1 m^2/g was obtained at a wavelength of 405 nm on June 7, 2023, which is consistent with that of fresh brown carbon emitted from wood combustion[44], as well as PM from peri-urban forest fires in Greece[45]. In addition, the WFPM *MAC* measured here is on par with those measured commonly from fresh WFPM[35] or brown carbon[43,46] with similar EC/OC content and range from 0.3 to 0.95 m^2/g. The good agreement between the *MAC* measured here for the entire WFPM and that measured in literature only for brown carbon indicates that the WFPM that arrived in the New Jersey/New York City area on June 7 contained mostly brown carbon particles that had not been photobleached completely, despite covering a distance of about 800 km. This is in line with the air transport modeling done here showing that air
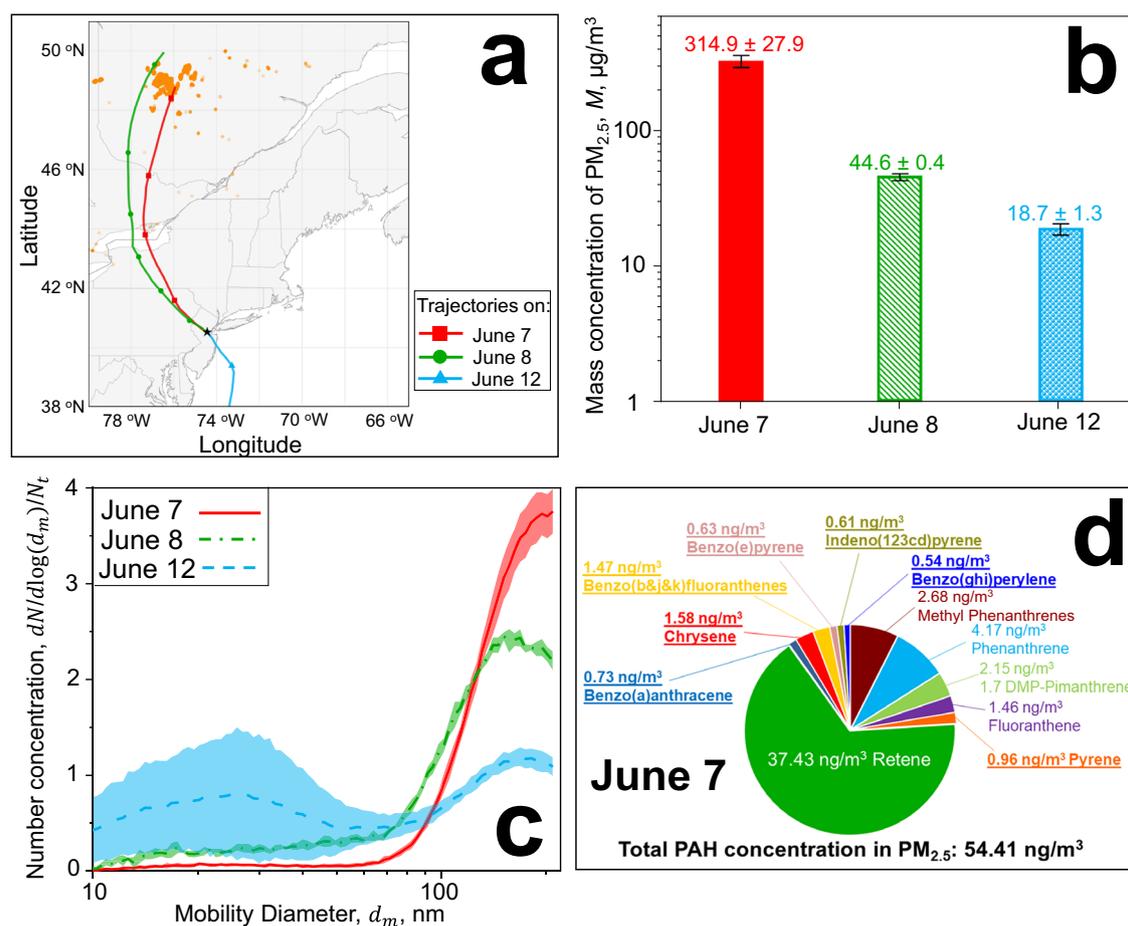
Fig. 1 | Transport and physicochemical properties of WFPM. Air mass trajectories (**a**) derived for June 7 (red squares), 8 (green circles) and 12 (blue triangles) along with the Canadian wildfire spots (orange circles) and the sampling site at Rutgers University campus (star). Lines connecting consecutive trajectory points represent 6 h of air mass transport (see Methods section). Mass concentrations, M, of $PM_{2.5}$ (**b**) along with mobility size distributions (**c**) measured on June 7 (red filled bar & solid line), 8 (green lined bar & dot-broken line) and 12 (blue dotted bar & broken line). The error bars and shaded areas quantify the variations of M and mobility size distributions during the measurement campaign. Concentrations of polycyclic aromatic hydrocarbons (PAHs) adsorbed on $PM_{2.5}$ sampled on June 7 (**d**). Error bars and shaded areas show the standard deviation of the mass concentration and mobility size distribution during the sampling period.

masses from the Canadian wildfires arrived within 24 h on June 7, with a large portion of this time being overnight.

In this regard, the *MAC* obtained for WFPM on June 8 decreased to $0.18 \pm 0.07 \ m^2/g$ and was similar to that measured on a wildfire smoke-free day (June 12: $0.14 \pm 0.07 \ m^2/g$). This can be attributed to the longer transport time (~36 h) of the air mass from the Canadian wildfires reaching the Northeast US on that day compared to June 7. In particular, the air mass arriving at our sampling site on June 8 was exposed to about 24 h of sunlight. Brown carbon particles are completely photobleached within 24 h of exposure to sunlight and thus their light absorption is eliminated[21,22], even though low-volatility brown carbon particles can exhibit resistance to photobleaching[47]. The WFPM *MAC* measured on June 8 and 12 are in good agreement with those measured for aged WFPM emissions in California, US and Siberia[48].

The *MAC* and *SSA* of WFPM measured on June 7 during the peak of the incident are in good agreement with those derived by Mie theory based on the measured mobility size distribution and EC/OC ratio (Fig. 2c, d: yellow open bars). This validates the present Mie theory calculations using a refractive index of 1.55–0.017i which is in line with those obtained for brown carbon particles having similar EC/OC content[19]. The small discrepancy between the measured (filled bar) and estimated (open bar) *SSA* can be attributed to the presence of particles larger than 2.5 μm that may contribute to light scattering and affect the measured *SSA*.

It should be noted that the WFPM measured here consists of inorganic species in addition to EC and OC[49]. The comparison of the measured WFPM *MAC* and *SSA* to those estimated using well-established refractive indexes[41] for EC and OC is still useful though, as it indicates which species affect mostly the WFPM optical properties. In particular, the excellent agreement between the measured WFPM *MAC* and that estimated for particles with the same EC/OC content indicates that the light absorption of WFPM is largely determined by its EC and OC. In contrast, the small deviation between the measured WFPM *SSA* and the estimated one suggests that the inorganic components of WFPM further increase its light scattering.

Radiative cooling by WFPM

The impact of WFPM on the regional microclimate is quantified by its instantaneous direct *RF* (Fig. 3) derived using the library for Radiative Transfer calculations[50] based on the *MAC* and *SSA* measured on June 7, 8 and 12 (Fig. 2c, d) and the vertically-integrated PM concentrations, C, derived by High-Resolution Rapid Refresh (HRRR; Fig. S3). The instantaneous direct *RF* obtained here are valid for the afternoon period during which the measurements were made. As expected, *RF* is negative for all these three days, as WFPM and background aerosols mostly scatter light having *SSA* close to 1 (Fig. 2d) with significantly lower values during the peak of the event on June 7.
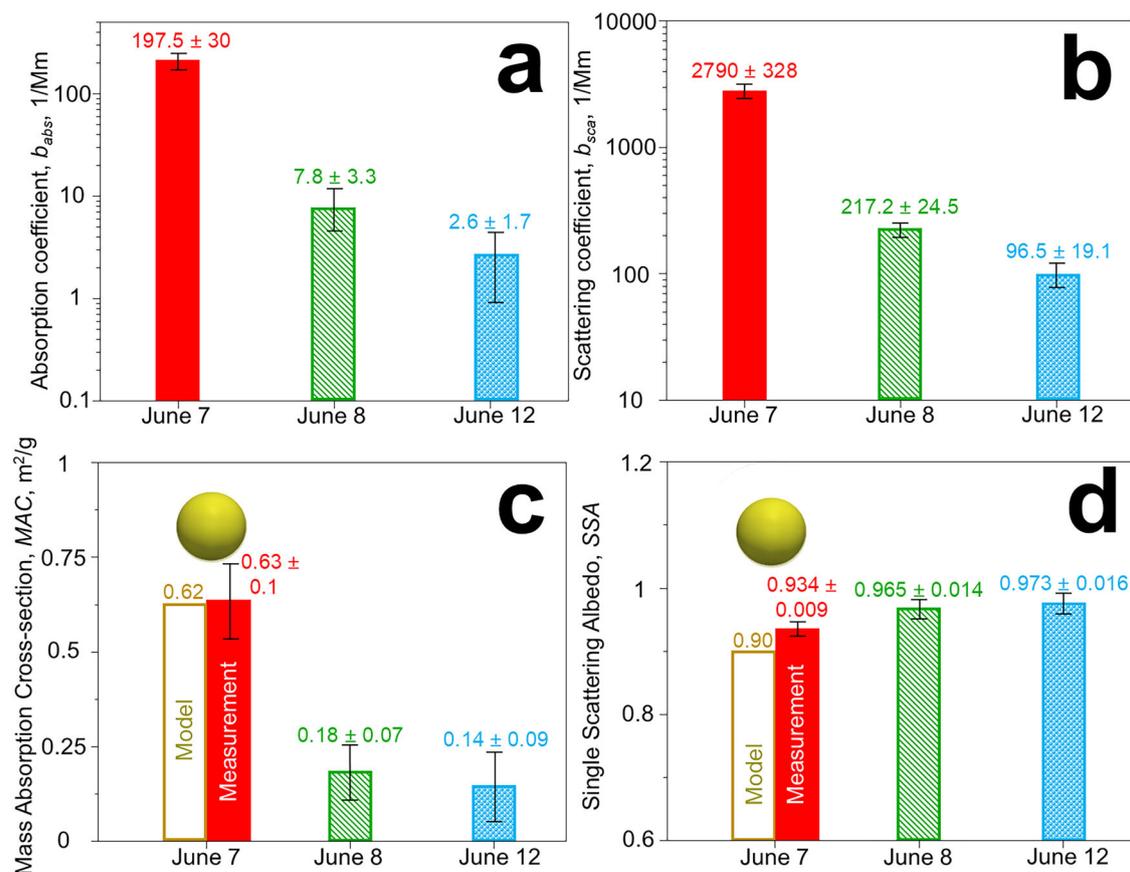
Fig. 2 | Optical properties of WFPM. Time-averaged absorption, b_{abs} (**a**), and scattering, b_{sca} (**b**), coefficients along with the respective mass absorption cross-section, MAC (**c**), and single scattering albedo, SSA (**d**), measured on June 7 (red filled bars), 8 (green lined bars) and 12 (blue dotted bars). The error bars quantify the variation of the WFPM optical properties during the measurement campaign. The standard deviations of the MAC and SSA were calculated based on those of the measured b_{abs} and b_{sca}. The MAC and SSA measured on June 7 are compared to those derived by Mie theory based on the measured mobility size distribution and EC/OC content (yellow open bars). The transport time of WFPM on June 7 and 8 was about 24 and 36 h, respectively. Error bars show the standard deviation of b_{abs}, b_{sca}, MAC and SSA during the sampling period.
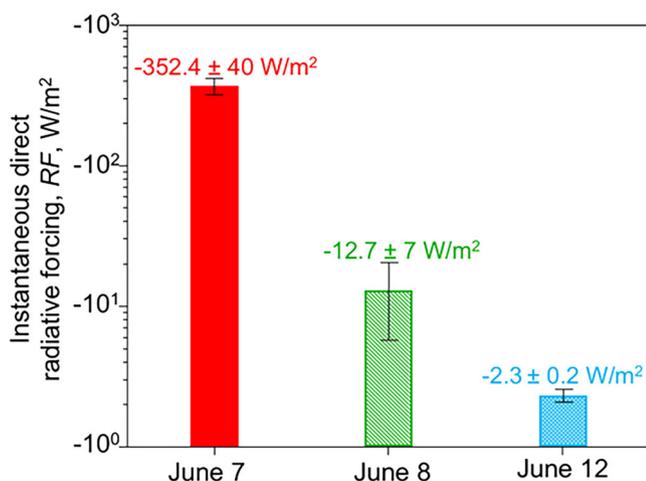

Fig. 3 | Radiative cooling induced by WFPM. Instantaneous direct radiative forcing, RF, estimated by libRadtran on June 7 (red filled bars), 8 (green lined bars) and 12 (blue dotted bars). Error bars show the RF standard deviation during the sampling period.

The large mass concentrations of WFPM arriving in the New Jersey/New York City area on June 7 resulted in strong radiative cooling and ambient air temperature reduction. In particular, the RF from WFPM sampled on June 7 resulted in direct RF of -352.4 ± 40 W/m². The direct RF estimated here for June 7 based on the measured WFPM optical properties is on par with that obtained by climate modeling during the Canadian wildfire incident in Northeast US[51]. This large radiative cooling is caused by the light scattered by WFPM away from the Earth surface, as well as by the energy absorbed and removed from the atmosphere[52]. The large direct $RF = -352.4$ W/m² obtained here for June 7 is based on the measured WFPM optical properties, while the modeling study of Wang et al.[51] reported a direct RF of about -100 W/m² relying on assumptions regarding the light absorption and scattering by WFPM. These assumptions resulted in substantial underestimation of the observed PM concentration and aerosol optical depth (as clearly shown in Fig. S9 of ref. 51). This explains the discrepancy between the direct RF reported here and that simulated by Wang et al.[51].

The large negative RF of WFPM can explain, at least to some extent, the temperature reduction of about 3 °C obtained based on meteorological data of the daily temperature for metropolitan areas in New Jersey and New York City during the peak of the Canadian wildfire incident (Fig. 4). It should be noted that weather patterns and indirect effects[53] from WFPM can not be ruled out as confounders of the observed temperature reduction.

On June 8, the WFPM light absorption and scattering decreased due to photobleaching, while C was also reduced. So, the radiative cooling induced by aged and photobleached WFPM sampled on June 8 is significantly lower compared to those from rather fresh WFPM sampled on June 7. Still, the large negative RF of WFPM on June 7 and 8 is 1–2 orders of magnitude larger than that obtained for background aerosols on June 12.

Implications for the microclimate of megacities and potential health effects

In this study, the physicochemical properties and radiative effects of WFPM from Canadian forest fires transported to the New Jersey/New York City metropolitan areas in June 2023 were analyzed. It was shown that WFPM contained primarily brown carbon particles that were transported far (800 km) from the area of the Canadian wildfires within 24 h with limited photobleaching and aging due to the rapid atmospheric transportation. More specifically, the light absorption strength (*MAC*) of WFPM sampled on June 7 (peak) was about a factor of three larger than those obtained from more "aged" WFPM on June 8, as well as from background aerosols on a wildfire smoke-free day (June 12).

Most importantly, the direct *RF* induced by WFPM was derived based on the light absorption and scattering measured in real time. At the peak of this Canadian wildfire incident (June 7), WFPM resulted in large negative direct *RF* of -352.4 ± 40 W/m^2, explaining to some extent the temperature reduction of about 3 °C observed in New Jersey/ New York City area (Fig. 4). While negative *RF* has been measured for high altitudes and reported in the literature for PM$_{2.5}$ from wildfires in Russia[23,24] and central US[25], this is the first time that strong radiative cooling by WFPM is measured in a densely populated megacity metropolitan area. The radiative cooling induced by WFPM in metropolitan areas of Northeast US has been also estimated at the top of the atmosphere based on climate modeling[51], while the optical properties of WFPM were measured in this work at ground level. Still, the direct *RF* estimated here for June 7 based on the measured WFPM optical properties is on par with that obtained by climate modeling during the Canadian wildfire incident in Northeast US[51].

The observed ambient air temperature reduction of about 3 °C is on par with those derived for PM from heavy air pollution in Chinese metropolitan areas[54], as well as with those derived by climate models for WFPM in western US[15]. Such ambient air temperature reductions may limit the urban heat island effect[54] and thus the natural ventilation of megacities. This may result in an increase of the residence time of WFPM near ground level, exacerbating the concentrations of air pollutants from other sources. This implication is corroborated by previous modeling and airplane measurements showing that brown carbon particles from wildfires remain largely at low altitudes and cool the atmosphere[25]. It is worth noting that such an increase of the residence time of wildfire smoke near ground level can be detrimental for public health, as the large concentrations of WFPM measured here substantially exceeded US National Ambient Air Quality Standard levels and the reduction of natural ventilation can increase concentrations of other air pollutants from other sources as well.

Finally, the unique chemistry of WFPM which contains large amounts of carcinogenic PAHs, raises further concerns for potential health effects which are reflected in recently published epidemiological studies in NYC[26–28]. Lung deposition modeling showed that about 4.5 mg of PM$_{2.5}$ were deposited in the respiratory system of people exposed for 72 h to WFPM during the Canadian wildfire incident in summer 2023[49], raising concerns for potential health outcomes. The measured exposure levels to WFPM, carcinogenic PAHs and other chemical components are presented in detail in an accompanying publication[49], while their potential toxicological impacts will be analyzed in future mechanistic studies using WFPM sampled during this episode.

In sum, this study quantifies the effects of climate-driven wildfires on the microclimate of a densely populated metropolitan area. Our findings confirm the negative *RF* that reduce the ground level air temperature and can compromise the natural ventilation of megacities resulting in higher concentrations of air pollutants and elevated risk for adverse health effects. Finally, it is clear that the systematic characterization of wildfire smoke transport and aging is essential for developing predictive models for the physicochemical properties of WFPM that are directly linked to its toxicological footprint.

Methods

Description of the sampling site

The physicochemical properties of WFPM were monitored at the Rutgers University Piscataway Campus, approximately 70 km southwest of New York City. A schematic of the instrumentation used here is shown in Fig. S1. Real time PM monitoring and time integrated PM sampling equipment were placed at the courtyard adjacent to the Environmental and Occupational Health Sciences Institute (EOHSI) at a sampling height 1.5 m above ground level. So, the WFPM mobility size distribution and optical properties were obtained during the wildfire incident on June 7 and 8, 2023, as well as after the incident on June 12, 2023. The real-time PM monitoring took place continuously for about one hour within the time frame of 14:30-17:00 (EST) on all three campaigns. This sampling period covered the peak of the wildfire incident on June 7[49]. During this period, the largest PM concentration was reported in New Jersey and New York states (see, for example, Fig. 2 in ref. 49). The same time period was used on June 8 and 12 for consistency.

Time-integrated WFPM sampling was also done on June 7 from 15:00 till 19:06. In addition, the mass concentration, *M*, of PM$_{2.5}$ on June 7, 8 and 12 averaged between 15:00 and 17:00 were obtained from the US EPA Photochemical Assessment Monitoring Station (AQS Site Code 340230011) that is located 12 km from the monitoring site.

Real-time monitoring of WFPM size distribution & optical properties

The mobility size distribution of WFPM is monitored using a Differential Mobility Analyzer Sizer (DMA 3085, TSI Inc., Shoreview, MN) coupled
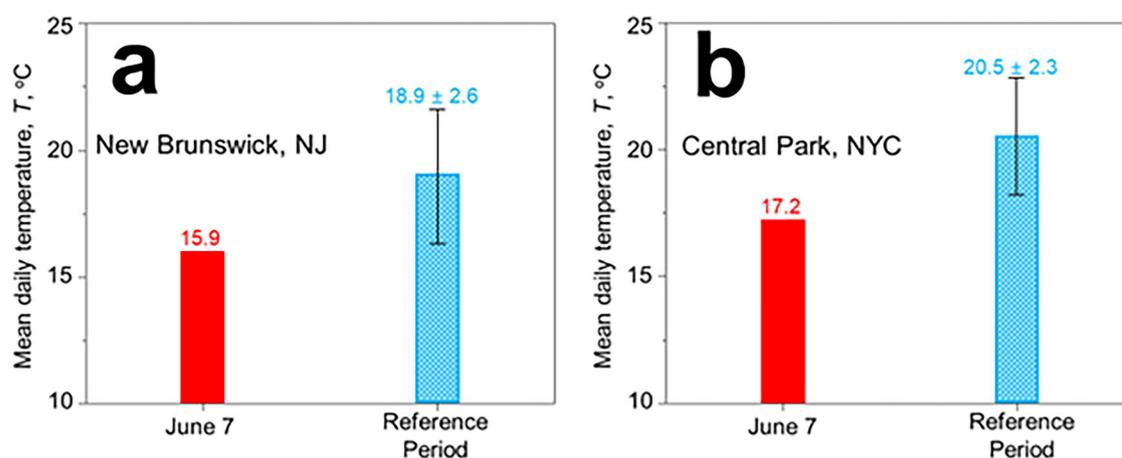

Fig. 4 | Impact of WFPM on ground level temperature of metropolitan areas in northeast US. Mean daily temperature, *T*, obtained based on meteorological data in New Brunswick, NJ (**a**) or Central Park, NYC (**b**) on June 7 (red filled bars) and the reference[27] smoke-free period (May 30–June 1 and June 12–14; blue dotted bars). Error bars show the standard deviation of the mean daily temperature during the reference period.

with a Condensation Particle Counter (CPC 3785, TSI Inc., Shoreview, MN) to measure in real-time particle number concentrations in the 5–300 nm mobility diameter range. A photoacoustic extinctionmeter (PAX, Droplet Measurement Technologies) is also used to sample and characterize WFPM. That way, its absorption, b_{abs}, and scattering, b_{sca}, coefficients at a wavelength of 405 nm are monitored every 1 s. The b_{abs} and b_{sca} measurement range of PAX is 1 Mm^{-1}. Despite some of the b_{abs} measured on June 12 were outside the measurement range, they were still included in the estimation of the average $<b_{abs}>$ to avoid any bias. The WFPM b_{abs} and b_{sca} can also be monitored using an aethalometer[48]. The evolution of b_{abs} and b_{sca} as a function of time during the sampling campaign is given in Fig. S4. The average mass absorption cross-section, MAC, is obtained using the $<b_{abs}>$ and $<M>$ averaged over 1 h:[43]

$$MAC = <b_{abs}>/<M> \qquad (1)$$

It should be noted that many studies report the brown carbon MAC by dividing the absorption coefficient by the OC mass concentration[44] and not the total PM concentration (as done in Eq. 1). Emissions from biomass burning are typically composed of 50–80% carbonaceous aerosols (EC and OC), and the remaining consists of other inorganic species[55]. The average single scattering albedo, SSA, is derived based on $<b_{abs}>$ and $<b_{sca}>$:

$$SSA = <b_{sca}>/(<b_{abs}> + <b_{sca}>) \qquad (2)$$

Time-integrated, size-fractionated sampling and off-line characterization of WFPM

The WFPM sampled between 15:00 and 19:06 (EST) on June 7, 2023 was fractionated into $PM_{0.1}$, $PM_{0.1-2.5}$, $PM_{2.5-10}$, and $PM_{>10}$ aerodynamic size fractions (cutoff diameters given in µm) using a Compact Cascade Impactor (CCI)[56] developed by the authors. So, $PM_{0.1}$ was collected on pre-baked quartz fiber filters (Pallflex Tissuquartz filter: 47 mm diameter, Pall Corporation, Port Washington, NY), while the larger size fractions were collected on polyurethane foam (PUF) substrates. Time-integrated sampling using two CCIs[56] was done for a longer duration compared to real-time monitoring to collect enough WFPM mass for off-line physicochemical and toxicological characterization studies. The $PM_{2.5}$ mass concentrations obtained by the US EPA Photochemical Assessment Monitoring Station averaged between 14:30 and 17:00 on June 7, 8 and 12 are presented in Fig. 1 to be consistent with the sampling duration used in the real-time monitoring data. The $PM_{2.5}$ mass concentration obtained using the CCI at the sampling location based on gravimetric analysis[49] is in excellent agreement with that obtained by US EPA Photochemical Assessment Monitoring Station (Fig. S5). The standard deviation of the average $PM_{2.5}$ mass concentration obtained from the two CCIs is about 4% (see the respective error bar in Fig. S5), indicating negligible variations between the WFPM sampled by the two collocated CCIs.

The PAHs adsorbed on the sampled $PM_{0.1}$ and $PM_{0.1-2.5}$ size fractions were obtained using the protocol described in Tsiodra et al.[57] with slight modifications (see Supplementary Information). The analysis focused on the identification of 25 PAHs with molecular weight between 178 to 278 g/mol. The analysis of organic and elemental carbon (EC-OC) was done for the $PM_{0.1}$ size fraction using the thermal-optical transmission (TOT) technique with a Sunset carbon analyzer (Sunset Laboratory Inc., Portland, OR, USA) and the EUSAAR2 thermal protocol described in detail by Cavalli et al.[58]. Since the $PM_{0.1}$ size fraction is used for the total carbon analysis, a fraction of the carbonaceous aerosols may have been missed, affecting the measured EC/OC ratio.

Wildfire smoke transport modeling

Backward air mass trajectories during the wildfire incident were obtained using the US National Oceanic and Atmospheric Administration, Air Resources Laboratory (NOAA-ARL) Hybrid Single-Particle Langrangian Integrated Trajectory (HYSPLIT) transport and dispersion model[59,60]

interfaced with the High-Resolution Rapid Refresh (HRRR) model that employs the Weather Research and Forecasting (WRF) system combined with observational data assimilation[61]. So, the backward trajectories of air arriving at the Rutgers monitoring site on June 7, 8 and 12 at 15:00 (EST) at about 500 m were derived for up to 24–36 h. The atmospheric height level of 500 m was used here to be close to sampling level, while avoiding inaccuracies from turbulence and frictional effects at lower heights[62]. Here, HYSPLIT simulations with HRRR and WRF were used to obtain indicative WFPM trajectories and aging times. Using GDAS instead of HRRR and WRF results in a similar aging time of about 24 h on June 7 and does not affect the interpretation of the experimental data presented here.

The column-integrated PM concentrations were directly derived from the vertical PM distributions using the HRRR smoke model. This model uses 51 cell layers in the vertical direction, consistent with the HRRR weather model. This configuration employs a hybrid pressure-sigma vertical coordinate system, transitioning from terrain, following sigma coordinates near the surface to isobaric coordinates at higher altitudes. Therefore, the column-integrated PM concentration was estimated by summing up PM masses in the cells above the specified location across all 51 cell layers of the HRRR smoke model. The vertical profiles of the PM mass concentrations were derived directly from the HRRR outputs without any assumption involved. Exemplary vertical concentration profiles obtained on June 7, 8 and 12 are presented in Fig. S6. The boundary layer PM concentration of 271.8 ± 47.4 µg/m^3 derived by HRRR smoke at 8 m above ground for June 7 is in good agreement with the measured 314.9 ± 27.9 µg/m^3. In contrast, the HRRR-derived concentrations of 16 ± 7.1 and 5.3 ± 0.7 and µg/m^3 obtained for June 8 and 12, respectively, are 64–72% smaller than those measured on those days.

Modeling of WFPM optical properties and radiative forcing

The light absorption and scattering of WFPM spheres with mobility diameter, d_m = 100–500 nm were derived using the Mie theory for spheres[63] using Maetzler's MATLAB code[64]. The refractive index, $RI = 1.55–0.017i$ at a wavelength, $\lambda = 405$ nm was obtained by averaging the indices of OC ($RI = 1.55$)[65] and young (H-rich) EC ($RI = 1.48–0.43i$)[41] based on the EC/OC measured on June 7, 2023 (Fig. S2). The WFPM MAC and mass scattering cross-section, MSC, were estimated based on the Mie-derived absorption, Q_{abs}:[42]

$$MAC = 1.5Q_{abs}/(d_m\rho) \qquad (3)$$

and scattering efficiency, Q_{sca}:[42]

$$MSC = 1.5Q_{sca}/(d_m\rho) \qquad (4)$$

where $\rho = 1.31$ g/cm^3 is the WFPM bulk density obtained by averaging those of OC ($\rho = 1.3$ g/cm^3)[66] and young EC ($\rho = 1.5$ g/cm^3)[67] based on the measured EC/OC. The WFPM SSA was obtained based on the Mie-derived Q_{abs} and Q_{sca}:[68]

$$SSA = Q_{sca}/(Q_{abs} + Q_{sca}) \qquad (5)$$

Since the WFPM MAC and SSA could be measured by PAX only at $\lambda = 405$ nm, the WFPM optical properties were also simulated at $\lambda = 266–848$ nm using the Mie theory and λ-dependent RI for freshly-emitted spheres[41] having the same EC/OC with the WFPM measured here. The MAC derived by Mie theory at $\lambda = 405$ nm is in excellent agreement with the experimental data, validating the present simulations (Fig. 2c). So, the wavelength dependence of the of the WFPM MAC and MSC derived by Mie theory were quantified using the absorption and scattering Angstrom exponents, respectively (Fig. S7a). It should be noted that the RI used here does not account for inorganic particles that are present in the WFPM[49]. This may limit the accuracy of the estimated MAC and MSC extrapolated at other wavelengths.

The d_m distribution of WFPM measured on June 7 is fitted with a lognormal size distribution to obtain the number concentration of particles with d_m = 400 and 500 nm. Relative fractions of 0.11, 0.45, 0.29, 0.11 and 0.04 were derived for WFPM particles with d_m = 100, 200, 300, 400 and 500 nm, respectively, by dividing their individual number concentrations by their summation. So, the average *MAC*, *MSC* and *SSA* were estimated based on those derived by Mie theory for particles with d_m = 100, 200, 300, 400 and 500 nm and the respective relative fractions. The mobility size distribution was also discretized in 10 and 20 size bins. Increasing the size bins from 5 to 20 hardly affects the estimated *MAC* and *SSA* (Fig. S8).

The direct radiative forcing, *RF*, of WFPM was derived using the UVSPEC model of the library for Radiative Transfer (libRadtran) package[50] with the 4-stream DIScrete Ordinates Radiative Transfer (DISORT) solver[69]. The solar irradiance at the top of the atmosphere (TOA) was estimated based on the synthetic spectral profile of Gueymard[70]. The radiative transfer calculations were performed for the spectral range between 300 and 3000 nm, employing the medium-resolution representative wavelength approach (REPTRAN) band parametrization[71]. The model accounts for the scattering and absorption of solar radiation by aerosols and atmospheric gases, as well as the reflection from the Earth's surface using a surface albedo of 0.183[72]. The surface albedo used here is considered a global mean value[72], but is still in good agreement with the 0.15-0.20 values reported for New Jersey[73]. The aerosol optical properties required for the radiative transfer calculations were the spectrally resolved aerosol optical depth (given by multiplying *MAC* by *C*), *SSA* and asymmetry parameter, *g*, which was used to calculate the phase function moments based on the Henyey–Greenstein approximation[71]. The WFPM *MAC* and *SSA* measured at λ = 405 nm, as well as the absorption and scattering Angstrom exponents and *g* (Fig. S7) derived by Mie theory were interfaced with the radiative transfer calculations to obtain spectrally-resolved optical properties. By contrasting the simulated net (downwelling – upwelling) hourly solar fluxes at the Earth's surface with and without PM, the instantaneous direct *RF* was obtained for the WFPM and background aerosols sampled on June 7, 8 and 12, 2023. The daily average direct *RF*, as well as its standard deviation were estimated based on the variation of the WFPM optical properties during the sampling campaign.

The daily mean temperatures obtained from the meteorological stations in New Brunswick, NJ[74] and Central Park, NYC[75] on June 7 are reported and compared to those measured during the reference wildfire smoke-free period (May 30-June 1 and June 12–14, 2023; Fig. 4). This period was chosen to be consistent with the reference (control) periods used in epidemiological studies of this wildfire incident in New York City[27]. In particular, wildfire smoke free periods before and after the wildfire incident are selected to minimize the impact of seasonal temperature variations that may take place within a period of two weeks.

Reporting summary
Further information on research design is available in the Nature Portfolio Reporting Summary linked to this article.

Data availability
The experimental data used to generate the figures of this article and its supplementary information can be found in a public repository[76].

Code availability
The codes used for the estimation of the WFPM transport (HRRR[59–61]) and radiative forcing (libRadtran package[50]) are open source and can be accessed through the web without any restrictions. The version of Maetzler's MATLAB code used here for Mie theory calculations is given in a public repository[76].

References
1. Jones, M. W. et al. Global and regional trends and drivers of fire under climate change. *Rev. Geophys.* **60**, (2022). e2020RG000726.
2. Ditas, J. et al. Strong impact of wildfires on the abundance and aging of black carbon in the lowermost stratosphere. *PNAS* **115**, E11595–E11603 (2018).
3. Reid, C. E. et al. Critical review of health impacts of wildfire smoke exposure. *Environ. Health Persp.* **124**, 1334–1343 (2016).
4. Hung, W. T. et al. The impacts of transported wildfire smoke aerosols on surface air quality in New York State: a case study in summer 2018. *Atmos. Environ.* **227**, 118513 (2020).
5. Andreae, M. O. & Gelencsér, A. Black carbon or brown carbon? The nature of light-absorbing carbonaceous aerosols. *Atmos. Chem. Phys.* **6**, 3131–3148 (2006).
6. Kelesidis, G. A., Goudeli, E. & Pratsinis, S. E. Morphology and mobility diameter of carbonaceous aerosols during agglomeration and surface growth. *Carbon* **121**, 527–535 (2017).
7. China, S., Mazzoleni, C., Gorkowski, K., Aiken, A. C. & Dubey, M. K. Morphology and mixing state of individual freshly emitted wildfire carbonaceous particles. *Nat. Commun.* **4**, (2013). 2122.
8. Li, W. J. et al. Microphysical properties of atmospheric soot and organic particles: measurements, modeling, and impacts. *Npj Clim. Atmos. Sci.* **7**, 65 (2024).
9. Chakrabarty, R. K. et al. Shortwave absorption by wildfire smoke dominated by dark brown carbon. *Nat. Geosci.* **16**, 683–688 (2023).
10. Vicente, A. et al. Organic speciation of aerosols from wildfires in central Portugal during summer 2009. *Atmos. Environ.* **57**, 186–196 (2012).
11. Wentworth, G R., Aklilu, Y. A., Landis, M. S. & Hsu, Y. M. Impacts of a large boreal wildfire on ground level atmospheric concentrations of PAHs, VOCs and ozone. *Atmos. Environ.* **178**, 19–30 (2018).
12. Verma, V. et al. Physicochemical and toxicological profiles of particulate matter in Los Angeles during the October 2007 southern california wildfires. *Environ. Sci. Technol.* **43**, 954–960 (2009).
13. Khraishah, H. et al. Climate change and cardiovascular disease: implications for global health. *Nat. Rev. Cardiol.* **19**, 798–812 (2022).
14. Schuller, A. & Montrose, L. Influence of woodsmoke exposure on molecular mechanisms underlying Alzheimer's disease: existing literature and gaps in our understanding. *Epigenet Insights* **13**, (2020). 2516865720954873.
15. Kochanski, A. K. et al. Modeling wildfire smoke feedback mechanisms using a coupled fire-atmosphere model with a radiatively active aerosol scheme. *J. Geophys. Res.-Atmos.* **124**, 9099–9116 (2019).
16. Zhang, A. X. et al. Modeling the global radiative effect of brown carbon: a potentially larger heating source in the tropical free troposphere than black carbon. *Atmos. Chem. Phys.* **20**, 1901–1920 (2020).
17. Kelesidis, G. A., Neubauer, D., Fan, L. S., Lohmann, U. & Pratsinis, S. E. Enhanced light absorption and radiative forcing by black carbon agglomerates. *Environ. Sci. Technol.* **56**, 8610–8618 (2022).
18. Yu, P. F. et al. Black carbon lofts wildfire smoke high into the stratosphere to form a persistent plume. *Science* **365**, 587–590 (2019).
19. Saleh, R. et al. Brownness of organics in aerosols from biomass burning linked to their black carbon content. *Nat. Geosci.* **7**, 647–650 (2014).
20. Shetty, N. et al. Brown carbon absorptivity in fresh wildfire smoke: associations with volatility and chemical compound groups. *Environ. Sci.-Atmos.* **3**, 1262–1271 (2023).
21. Forrister, H. et al. Evolution of brown carbon in wildfire plumes. *Geophys. Res. Lett.* **42**, 4623–4630 (2015).
22. Schnitzler, E. G. et al. Rate of atmospheric brown carbon whitening governed by environmental conditions. *PNAS* **119**, e2205610119 (2022).

23. Péré, J. C. et al. Direct radiative effect of the Russian wildfires and its impact on air temperature and atmospheric dynamics during August 2010. *Atmos. Chem. Phys.* **14**, 1999–2013 (2014).

24. Konovalov, I. B. et al. Application of the CHIMERE-WRF model complex to study the radiative effects of siberian smoke aerosol in the Eastern Arctic. *Atmos. Ocean Opt.* **36**, 337–347 (2023).

25. Zhang, Y. Z. et al. Top-of-atmosphere radiative forcing affected by brown carbon in the upper troposphere. *Nat. Geosci.* **10**, 486–489 (2017).

26. Thurston, G., Yu, W. Y. & Luglio, D. An evaluation of the asthma impact of the June 2023 New York City wildfire air pollution episode. *Am. J. Resp. Crit. Care* **208**, 898–900 (2023).

27. Chen, K., Ma, Y. Q., Bell, M. L. & Yang, W. Canadian Wildfire Smoke and Asthma Syndrome Emergency Department visits in New York City. *Jama-J. Am. Med Assoc.* **330**, 1385–1387 (2023).

28. Meek, H. C. et al. Asthma-Associated Emergency Department visits during a wildfire smoke event—New York. *Mmwr-Morb. Mortal. W* **72**, 933–935 (2023). June 2023.

29. Ramdahl, T. Retene—a molecular marker of wood combustion in ambient air. *Nature* **306**, 580–583 (1983).

30. Peixoto, M. S. et al. Oxidative stress, mutagenic effects, and cell death induced by retene. *Chemosphere* **231**, 518–527 (2019).

31. Samburova, V. et al. Polycyclic aromatic hydrocarbons in biomass-burning emissions and their contribution to light absorption and aerosol toxicity. *Sci. Total Environ.* **568**, 391–401 (2016).

32. Liu, B., Xue, Z. Q., Zhu, X. L. & Jia, C. R. Long-term trends (1990-2014), health risks, and sources of atmospheric polycyclic aromatic hydrocarbons (PAHs) in the US. *Environ. Pollut.* **220**, 1171–1179 (2017).

33. Lack, D. A. et al. Brown carbon and internal mixing in biomass burning particles. *PNAS* **109**, 14802–14807 (2012).

34. Selimovic, V., Yokelson, R. J., McMeeking, G. R. & Coefield, S. In situ measurements of trace gases, PM, and aerosol optical properties during the 2017 NW US wildfire smoke event. *Atmos. Chem. Phys.* **19**, 3905–3926 (2019).

35. Carter, T. S. et al. Investigating carbonaceous aerosol and its absorption properties from fires in the Western United States (WE-CAN) and Southern Africa (ORACLES and CLARIFY). *J. Geophys. Res.-Atmos.* **126**, e2021JD034984 (2021).

36. May, A. A. et al. Aerosol emissions from prescribed fires in the United States: a synthesis of laboratory and aircraft measurements. *J. Geophys. Res.-Atmos.* **119**, 11826–11849 (2014).

37. Haynes, J. P., Miller, K. E. & Majestic, B. J. Investigation into photoinduced auto-oxidation of polycyclic aromatic hydrocarbons resulting in brown carbon production. *Environ. Sci. Technol.* **53**, 682–691 (2019).

38. Liu, S. et al. Aerosol single scattering albedo dependence on biomass combustion efficiency: Laboratory and field studies. *Geophys. Res. Lett.* **41**, 742–748 (2014).

39. Laing, J. R., Jaffe, D. A. & Hee, J. R. Physical and optical properties of aged biomass burning aerosol from wildfires in Siberia and the Western USA at the Mt. Bachelor Observatory. *Atmos. Chem. Phys.* **16**, 15185–15197 (2016).

40. Sedlacek, A. J. et al. Formation and evolution of tar balls from northwestern US wildfires. *Atmos. Chem. Phys.* **18**, 11289–11301 (2018).

41. Kelesidis, G. A., Bruun, C. A. & Pratsinis, S. E. The impact of organic carbon on soot light absorption. *Carbon* **172**, 742–749 (2021).

42. Kelesidis, G. A. & Pratsinis, S. E. Soot light absorption and refractive index during agglomeration and surface growth. *Proc. Combust. Inst.* **37**, 1177–1184 (2019).

43. Islam, M. M., Neyestani, S. E., Saleh, R. & Grieshop, A. P. Quantifying brown carbon light absorption in real-world biofuel combustion emissions. *Aerosol Sci. Technol.* **56**, 502–516 (2022).

44. Olson, M. R. et al. Investigation of black and brown carbon multiple-wavelength-dependent light absorption from biomass and fossil fuel combustion source emissions. *J. Geophys. Res.-Atmos.* **120**, 6682–6697 (2015).

45. Kaskaoutis, D. G. et al. Impact of peri-urban forest fires on air quality and aerosol optical and chemical properties: the case of the August 2021 wildfires in Athens, Greece. *Sci. Total Environ.* **907**, (2024). 168028.

46. Zhong, M. & Jang, M. Dynamic light absorption of biomass-burning organic carbon photochemically aged under natural sunlight. *Atmos. Chem. Phys.* **14**, 1517–1525 (2014).

47. Di Lorenzo, R. A. et al. Molecular-size-separated brown carbon absorption for biomass burning aerosol at multiple field sites. *Environ. Sci. Technol.* **51**, 3128–3137 (2017).

48. Laing, J. R., Jaffe, D. A. & Sedlacek, A. J. Comparison of filter-based absorption measurements of biomass burning aerosol and background aerosol at the Mt. Bachelor Observatory. *Aerosol Air Qual. Res.* **20**, 663–678 (2020).

49. Laurent, J. G. C. et al. Physicochemical characterization of the particulate matter in New Jersey/New York City area, resulting from the Canadian Quebec wildfires in June 2023. *Environ. Sci. Technol.* **58**, 14753–14763 (2024).

50. Emde, C. et al. The libRadtran software package for radiative transfer calculations (version 2.0.1). *Geosci. Model Dev.* **9**, 1647–1672 (2016).

51. Wang, Z. L. et al. Intensification of mid-latitude cyclone by aerosol-radiation interaction increases transport of Canadian Wildfire Smoke to Northeastern US. *Geophys Res Lett.* **51**, (2024). e2024GL108444.

52. Chylek, P. & Wong, J. Effect of absorbing aerosols on global radiation budget. *Geophys. Res. Lett.* **22**, 929–931 (1995).

53. Zheng, G. J. et al. Long-range transported North American wildfire aerosols observed in marine boundary layer of eastern North Atlantic. *Environ. Int.* **139**, 105680 (2020).

54. Wu, H. et al. Urban heat island impacted by fine particles in Nanjing, China. *Sci. Rep.* **7**, (2017). 11422.

55. Andreae, M. O. Emission of trace gases and aerosols from biomass burning—an updated assessment. *Atmos. Chem. Phys.* **19**, 8523–8546 (2019).

56. Demokritou, P., Lee, S. J., Ferguson, S. T. & Koutrakis, P. A compact multistage (cascade) impactor for the characterization of atmospheric' aerosols. *J. Aerosol Sci.* **35**, 281–299 (2004).

57. Tsiodra, I. et al. Annual exposure to polycyclic aromatic hydrocarbons in urban environments linked to wintertime wood-burning episodes. *Atmos. Chem. Phys.* **21**, 17865–17883 (2021).

58. Cavalli, F., Viana, M., Yttri, K. E., Genberg, J. & Putaud, J. P. Toward a standardised thermal-optical protocol for measuring atmospheric organic and elemental carbon: the EUSAAR protocol. *Atmos. Meas. Technol.* **3**, 79–89 (2010).

59. Draxler, R. R. & Hess, G. D. An overview of the HYSPLIT_4 modelling system for trajectories, dispersion and deposition. *Aust. Meteorol. Mag.* **47**, 295–308 (1998).

60. Stein, A. F. et al. Noaa's Hysplit atmospheric transport and dispersion modeling system. *Bull. Am. Meteorol. Soc.* **96**, 2059–2077 (2015).

61. Benjamin, S. G. et al. A North American hourly assimilation and model forecast cycle: the rapid refresh. *Mon. Weather Rev.* **144**, 1669–1694 (2016).

62. Chen, L. W. A. et al. Analysis of a summertime PM and haze episode in the mid-Atlantic region. *J. Air Waste Manag.* **53**, 946–956 (2003).

63. Kelesidis, G. A., Nagarkar, A. & Rivano, P. G. Solar steam generation enabled by carbon black: the impact of particle size and nanostructure. *AIChE J.* **70**, e18619 (2024).

64. Maetzler, C. MATLAB Functions for Mie Scattering and Absorption, Research Report, University of Bern, Switzerland, omlc.org/software/mie/maetzlermie/Maetzler2002.pdf.

65. Chakrabarty, R. K. & Heinson, W. R. Scaling laws for light absorption enhancement due to nonrefractory coating of atmospheric black carbon aerosol. *Phys. Rev. Lett.* **121**, 218701 (2018).
66. Adler, G., Riziq, A. A., Erlick, C. & Rudich, Y. Effect of intrinsic organic carbon on the optical properties of fresh diesel soot. *PNAS* **107**, 6699–6704 (2010).
67. Camacho, J. et al. Mobility size and mass of nascent soot particles in a benchmark premixed ethylene flame. *Combust. Flame* **162**, 3810–3822 (2015).
68. Draine, B. T. & Flatau, P. J. Discrete-dipole approximation for scattering calculations. *J. Opt. Soc. Am. A* **11**, 1491–1499 (1994).
69. Buras, R., Dowling, T. & Emde, C. New secondary-scattering correction in DISORT with increased efficiency for forward scattering. *J. Quant. Spectrosc. Radiat. Transf.* **112**, 2028–2034 (2011).
70. Gueymard, C. A. The sun's total and spectral irradiance for solar energy applications and solar radiation models. *Sol. Energy* **76**, 423–453 (2004).
71. Henyey, L. G. & Greenstein, J. L. Diffuse radiation in the galaxy. *Astrophys J.* **93**, 70–83 (1941).
72. Hassan, T., Moosmüller, H. & Chung, C. E. Coefficients of an analytical aerosol forcing equation determined with a Monte-Carlo radiation model. *J. Quant. Spectrosc. Radiat. Transf.* **164**, 129–136 (2015).
73. Wichansky, P. S., Steyaert, L. T., Walko, R. L. & Weaver, C. P. Evaluating the effects of historical land cover change on summertime weather and climate in New Jersey: Land cover and surface energy budget changes. *J. Geophys Res* **113**, D10107 (2008).
74. Rutgers New Jersey Weather Network. https://www.njweather.org/station/1101.
75. National Weather Service. https://www.weather.gov/wrh/Climate?wfo=okx.
76. 4TU.ResearchData. https://doi.org/10.4121/963d23da-9d1d-4771-ab30-8b41de423c95; https://data.4tu.nl/private_datasets/EzDJDEdC1mVCrpCY5nGqoPPP3pALakjOSi9O5HIqfVc.

Author contributions
G.A.K.: Conceptualization, Methodology, Software, Validation, Formal analysis, Investigation, Resources, Writing—Original Draft, Writing—Review & Editing, Visualization, Supervision, Project administration. C.M.: Investigation, Writing—Review & Editing. H.P.: Investigation, Writing—Review & Editing. L.C.: Investigation, Writing—Review & Editing. I.T.: Methodology, Formal analysis, Investigation, Writing—Review & Editing. N.M.: Methodology, Formal analysis, Resources, Writing—Review & Editing, Supervision. I.K.: Methodology. M.B.K.C.: Methodology, Software, Formal analysis, Investigation, Writing—Review & Editing. N.H.: Methodology, Software, Formal analysis, Resources, Writing—Review & Editing, Supervision. P.G.G.: Methodology, Software, Formal analysis, Investigation, Resources, Writing—Review & Editing, Visualization. J.G.C.L.: Methodology, Writing—Review & Editing, Visualization, Supervision. P.D.: Conceptualization, Resources, Writing—Review & Editing, Supervision, Project administration.

Competing interests
The authors declare no competing interests.

Additional information
Supplementary information The online version contains supplementary material available at https://doi.org/10.1038/s43247-025-02214-3.

Correspondence and requests for materials should be addressed to Georgios A. Kelesidis or Philip Demokritou.

Peer review information *Communications Earth & Environment* thanks Hiep Nguyen Duc and the other, anonymous, reviewer(s) for their contribution to the peer review of this work. Primary Handling Editor: Alice Drinkwater. [A peer review file is available].

Reprints and permissions information is available at http://www.nature.com/reprints

Publisher's note Springer Nature remains neutral with regard to jurisdictional claims in published maps and institutional affiliations.